



Co-published by
Institute of Fluid-Flow Machinery
Polish Academy of Sciences
Committee on Thermodynamics and Combustion
Polish Academy of Sciences

Copyright©2024 by the Authors under license CC BY 4.0

<http://www.imp.gda.pl/archives-of-thermodynamics/>



Experimental investigation and performance prediction of SAH using different arc rib roughness geometries – A comparative study

Jitendra Singh^{a*}, Atul Lanjewar^a

^a MANIT, Bhopal 462033, India

*Corresponding author email: jitendrasinghbti285@gmail.com

Received: 24.02.2023; revised: 08.05.2023; accepted: 06.12.2023

Abstract

This study aims to investigate and compare the thermal performance of a solar air heater using a passive technique to enhance heat transfer between the absorber plate and the flowing fluid. The technique involves generating turbulence near the heat transferring surface through the use of artificial rib roughness. The study focuses on two different novel roughness geometries: full symmetrical arc rib roughness and half symmetrical arc rib roughness. By introducing additional gaps and varying the number of gaps in the roughness geometries, the study examines their effects on the solar air heaters thermal performance. The artificially roughened surface creates different turbulent zones, which are essential to the development of different types of turbulence in the vicinity of the heat transferring surface. The study finds that an optimal escalation in Nusselt number and friction factor by 2.36 and 3.45 times, respectively, occurs at certain gap numbers as 6 and n_g as 5 for full symmetrical arc rib roughness. The maximum thermal-hydraulic performance parameter of 1.66 is attained at a Reynolds number of 6 000. The study also conducts correlation, mathematical modeling, and performance prediction under different operating circumstances.

Keywords: Full/Half symmetrical arc rib; Additional gap; Nusselt number; Thermohydraulic performance parameter

Vol. 45(2024), No. 1, 33–44; doi: 10.24425/ather.2024.150436

Cite this manuscript as: Singh, J., & Lanjewar, A. (2024). Experimental investigation and performance prediction of SAH using different arc rib roughness geometries - A comparative study. *Archives of Thermodynamics*, 45(1), 33–44.

1. Introduction

The most realistic and cost effective, immeasurable and straightforward reachable active non-conventional source of energy is solar energy.

Any country's access to energy resources has a significant impact on its commercial and scientific development. To solve the issue of total dependence on traditional energy sources, the industry must be modernized [1]. Fossil fuel deterioration is a significant problem that occurs everywhere in the world. By using energy intelligently and shifting toward unconventional energy sources, demand and supply are kept in balance. Room

heating and ventilation, crop drying (for goods like tea, coffee, maize, fruits and vegetables) and aeration in the laundry sector are all uses of readily available solar energy [2].

Solar collectors, which convert solar radiation (including direct and indirect radiation) into heat energy and transmit it to a fluid, are an essential part of the solar air heater (SAH) system. Low SAH efficiency is brought on by the viscous sub-layer that covers the absorber plate. An effective method to disrupt the laminar sub-layer and raise the heat transfer coefficient h is to add rib components to the absorber surface [3]. The rib element in a roughened SAH generates turbulence at the absorber surface.

Nomenclature

A_p – absorber plate area, m²
 A_o – orifice area, m²
 C_d – orifice coefficient discharge
 C_p – specific heat of flowing fluid (air), J·kg⁻¹·K⁻¹
 D_h – hydraulic diameter, m
 d_1 – orifice pipe diameter, m
 d_2 – orifice diameter, m
 d/w – relative gap position
 e – rib thickness, m
 ee^+ – roughness Reynolds number
 e/D_h – rib height relative to hydraulic diameter
 fs – friction factor at smooth surface
 fr – friction factor at rough surface
 F_p – plate efficiency factor
 F_o – heat removal factor
 g – gap width, m
 g' – gap width of additional gap
 G – air mass velocity, kg·s⁻¹·m⁻²
 G' – heat transfer function
 g/e – gap width relative to rib height
 g'/e – gap width of additional gap relative to rib height
 H – duct height, m
 h – convective heat transfer coefficient, W·m⁻²·K⁻¹
 h_w – rate of heat loss due to wind, W·m⁻²·K⁻¹
 I – solar radiation intensity, W·m⁻²
 k – thermal conductivity, W·m⁻¹·K⁻¹
 k_i – thermal conductivity (insulation), W·m⁻¹·K⁻¹
 L – test length, m
 m – air mass flow rate, kg·s⁻¹
 N – Number of glass cover
 N_g – Number of symmetrical gaps over full arc
 n_g – Number of additional gaps on symmetrical elements
 Nu_r – Nusselt number at rough surface
 Nu_s – Nusselt number at smooth surface
 p – roughness pitch, m
 p' – staggered rib pitch, m
 p_{am} – atmospheric pressure, N·m⁻²
 p/e – roughness pitch relative to rib height
 p'/p – staggered rib pitch relative to roughness pitch
 Pr – Prandtl number

Q_u – useful heat gain through air, W
 R – roughness function
 Re – Reynolds number
 r – staggered rib size, m
 r/e – staggered rib length relative to rib height
 St – Stanton number of roughened plate
 t_e – edge thickness, m
 t_i – edge insulation thickness, m
 T_a – ambient temperature, K
 T_f – average air temperature, K
 T_i – initial temperature of air, K
 T_o – average outlet temperature of air, K
 T_p – average temperature of absorbing surface of the plate, K
 U_b – bottom heat loss coefficient, W·m⁻²·K⁻¹
 U_L – overall heat loss coefficient, W·m⁻²·K⁻¹
 U_s – side heat loss coefficient, W·m⁻²·K⁻¹
 U_t – top heat loss coefficient, W·m⁻²·K⁻¹
 V – air velocity in SAH duct, m·s⁻¹
 V_w – velocity wind, m·s⁻¹
 W – duct width, m
 W/H – aspect ratio

Greek symbols

α – angle of attack, degree
 β – orifice diameter to pipe diameter
 ρ_a – density at T_f , kg·m⁻³
 Δh_o – head difference at orifice plate, m
 Δp_d – pressure difference along the test section, N·m⁻²
 Δp_o – pressure difference across orifice plate, N·m⁻²
 μ – dynamic viscosity, P·as
 σ – Stefan Boltzmann constant
 ε_g – emissivity glass cover
 ε_p – emissivity absorber plate
 $\tau\alpha$ – transmissivity–absorptivity product
 η_{th} – thermal efficiency of solar air heater (SAH)
 δ – bottom insulation thickness
 η – thermohydraulic performance parameter (THPP)
 ΔT – augmentation in temperature across the duct, °C

Abbreviations and Acronyms

SAH – Solar Air Heater
 THPP – Thermohydraulic Performance Parameter

Although adding ribs to the absorber surface increases frictional losses, it also boosts the SAH system's effectiveness. The blower bills are increased by frictional losses as extra power is needed to create suction inside the duct so that fluid can flow as intended [4]. Many scientists have investigated the impacts of different rib designs on the heat transfer coefficient, the impact of friction factor on the pressure drop across the orifice meter (Δp_d) and thermal-hydraulic performance parameter (THPP) [5]. There is still a need to identify the best rib geometry - pattern, pitch and position for improved thermal and hydraulic performance.

The concept of rib roughness in a double pass SAH was applied to investigate the influence of discrete multi-V shaped and staggered rib on the performance of SAH [6]. Discrete multi-V shaped and staggered rib geometry performs better than discrete V-shaped with a staggered element [7]. A staggered V-shaped

twisted rib was investigated using the LCT technique to visualize the fluid flow [5]. The thermal efficiency of SAH was improved with the use of double glazed finned steel absorber plate [8]. Augmentation in heat transfer rate is observed while using petal shaped and a quarter cylinder rib in compression with a square rib [9]. An experimental investigation has been conducted to investigate the performance of SAH duct roughened with expended metal-mesh roughness geometry [10]. A medical glass panel was installed in between the two layers of glass instead of the metal plate in a double pass solar air heater [11]. An experimental investigation was carried out by taking gaps in V-rib roughness with a staggered element [12]. Numerical analysis was conducted with novel V rib geometry [13]. Literature reveals the effect of different roughness geometries in several orientations such as transverse, inclined, V-up continuous, V-down

continuous, V-up discrete and V-down discrete rib arrangement, and the reported V-down discrete geometry is the best over other investigated geometries [14].

Continuous arc-shaped rib geometry is basic arc geometry. Experimental analysis has evolved by modifying arc roughness geometry in sequential order. The basic is continuous arc-shaped parallel wire rib roughness geometry [15]. Significant enrichment in Nusselt (Nu) number and friction factor (f) has been reported with the use of arc shaped roughness geometry [16]. Full width arc of continuous arc geometry with gap performs better over continuous arc geometry in terms of the Nu number and friction factor [17]. An experimental investigation was carried out with a broken arc rib combined with a staggered rib piece and concluded that due the presence of the staggered rib element in the broken arc rib more turbulence was generated, which leads to a high value of Nu number and friction factor [18]. Experimental investigation was conducted with arc rib with multiple gap roughness geometry [19] and came to conclude that the performance of arc rib with multiple gaps is better than continuous arc geometry [16] and broken arc shaped rib geometry [18]. Novel discrete symmetrical arc rib geometry was experimentally investigated with the aspect ratio W/H as 8 [20]. Symmetrical gap arc geometry and staggered element [21] shows better enrichment in Nu and f in comparison of an arc rib with multiple gap roughness geometry [19]. The comparison of single discrete arc roughness and double discrete arc roughness reveals that double discrete arc roughness has a higher THPP [22]. Multiple arc shaped roughness geometry shows the maximum enrichment in Nu and f with the ratio W/w as 5 and W/w as 7, respectively [23]. An experimental investigation was conducted with the use of novel discrete double arc reverse geometry [24] as well as a multiple arc with a gap [25] and a discrete multiple arc rib [26] revealing the behaviour of the flowing fluid.

1.1. Research gap

On the basis of a wide literature survey analysis, the following can be inferred:

- 1). Performance improvement of the continuous arc rib can be achieved by the provision of a gap in the continuous arc rib. Secondary flow refreshment by gap provision takes place. Also, flow acceleration through the gap interrupts boundary layer growth downstream near the reattachment zone.
- 2). Enhancement in heat transfer coefficient can be achieved by placing a staggered element in front of the gap as compared to the gap in arc rib geometry. Placing staggered elements leads to vortices mixing with the main flow.
- 3). Further improvement can be anticipated by gap provision in a considerably long continuous arc segment as it has unhindered boundary layer growth along this continuous arc segment. Gap provision is expected to break this unhindered boundary layer growth due to flow acceleration in the gap. This additional gap in the continuous arc segment is a novelty as it has not been explored by researchers to this date in the literature. It will lead to the discretization of a continuous arc segment that can lead to a higher h value from the absorber plate to the flowing fluid by

shortening the symmetrical rib element length by giving an additional small gap that can reduce boundary layer formation as well as increase the flow acceleration. The purpose of this experimental study is to explore the discussed idea (providing an additional small gap) by using a discrete symmetrical arc rib with staggered rib roughness to see improvement in h and f values and also compare the performance of this improved SAH with that of smooth SAH.

4). As a result, experimental investigation of additional gaps in the present study (half symmetrical arc rib geometry and full symmetrical arc rib geometry) is necessary and its performance comparison to that of the existing best arc rib roughness geometry available in the literature [19] and [21]. If the performance is better, then providing an additional gap will indeed be a novelty.

5). Thus, the research gap manifests in improving the performance of existing best arc rib geometry by exploring the effect of an additional gap on a continuous arc segment of existing best arc rib roughness geometry available in the literature [19] and [21].

1.2. Objectives of the present study

The objectives of the present study are as follows:

- 1). To determine the effect of the main gap, additional symmetrical gap and staggered element of half symmetrical arc rib geometry and full symmetrical arc rib geometry on the heat transfer, pressure drop and THPP parameter of a roughened SAH duct.
- 2). To compare the THPP parameter of the proposed geometries with the existing best arc rib roughness geometry available in the literature [19] and [21].
- 3). To develop a correlation between the roughness function (R) and roughness Reynolds number (e^+) and heat transfer function (G') and roughness Reynolds number (e^+).

2. Experimental arrangement

The indoor test setup has been constructed as per ASHRAE, Standard [27] as illustrated in Fig. 1(a) for the experimental run of the roughened SAH duct. The test setup includes a control valve, blower, galvanised iron (GI) pipe, PVC hose pipe and a rectangular channel with an absorber plate on the top. Fig. 1(b) depicts a cross-sectional figure of the SAH duct channel. The indoor experimental duct which has the dimensions 2350 mm by 300 mm by 25 mm and a W/H ratio of 12 is shown in Fig. 1(c).

The experimental duct is 800 mm long at the inlet section, 1000 mm long at the test section and 550 mm long at the exit section. For adequate hot air mixing, baffles are implanted at the duct's exit section. As an absorber plate, a hot-rolled (1.2 mm thick) sheet with a span of 1000 mm is used. A test plate area of 1 000 mm by 300 mm is roughened using a copper wire with a 2 mm diameter and applied to improve absorptivity of black paint on the other side of the plate. An electric heater made of a nichrome wire emits a 1 000 W/m² constant heat flux over the absorber plate. A 50 mm thick thermocol is used to insulate the whole duct. A galvanized iron (GI) pipe is insulated from the

exit portion to the orifice plate. The customized insulating rope and plaster of paris are used to insulate the GI pipe.

To measure the mass flow rate (m) of the flowing fluid

within the rectangular duct a digital manometer is mounted across the orifice plate. A control valve is put before the centrifugal blower to adjust m in the test channel. T-type thermocouples are located at the entrance section to measure the ambient air temperature, temperature at the top surface of the absorber plate and the temperature of heated air at the exit section under steady-state conditions. To measure the temperature of ambient air a single thermocouple is placed at the entrance of the SAH duct and the temperature of hot air leaving the duct is measured with 5 thermocouples that are placed span-wise at the transition section. The data logger uses thermocouples to capture temperature readings. The Δp_d along the test portion is measured using a digital micro-manometer.

The optimal physiognomic behaviour of roughness geometries mentioned in [19], [21] and two different proposed roughness geometries, namely, half symmetrical arc rib geometry and full symmetrical arc rib geometry has been determined through experimental runs with a rectangular SAH duct (W/H ratio as 12).

The new geometry consists of a symmetrical arc segment with symmetrical gaps and additional gaps on symmetrical arc segments. The schematic and photographic representation of half symmetrical arc rib geometry and full symmetrical arc rib geometry is depicted in Fig. 2 and Fig. 3, respectively. Table 1 displays the roughness and performance metrics for the experimental inquiry.

3. Procedure of investigations

It is ensured that all the equipment is correctly connected and in operating condition before starting the experimental run. The

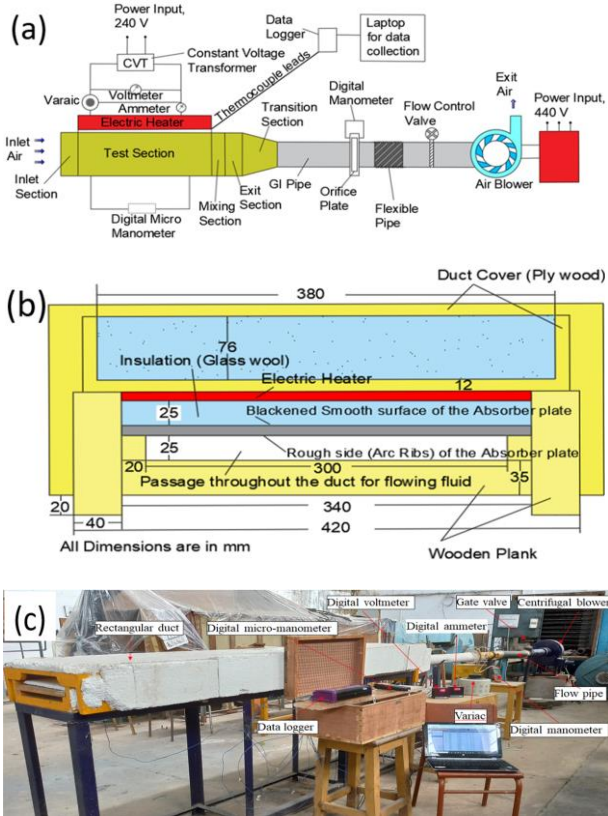


Fig. 1. (a) Outline of experimental set-up; (b) Cross-sectional view of rectangular duct; (c) Photograph of experimental set-up.

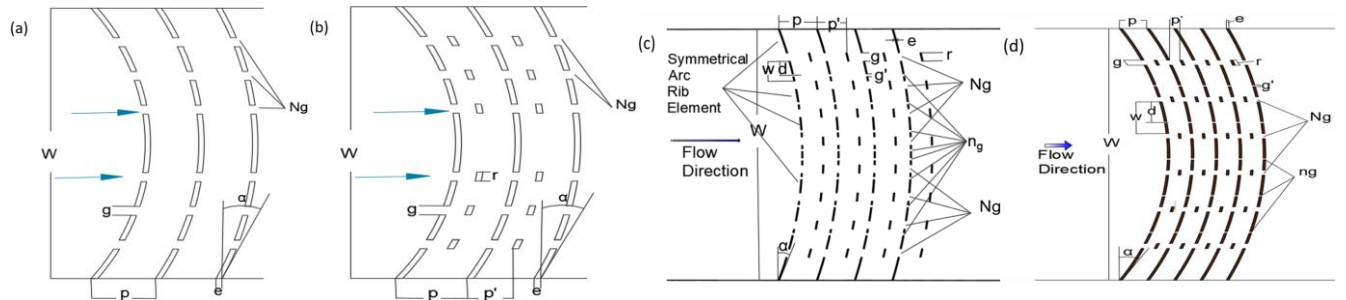


Fig. 2. Schematic view of different roughness geometries: (a) Arc rib with multiple gaps [19]; (b) Symmetrical gap arc geometry and staggered element [21]; (c) Half symmetrical arc rib geometry; (d) Full symmetrical arc rib geometry.

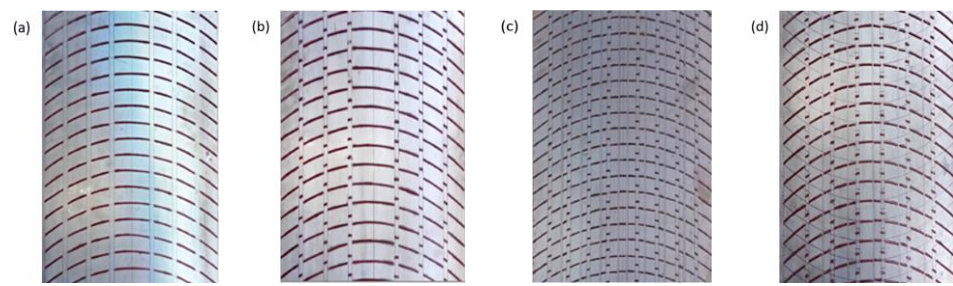


Fig. 3. Photographic view of different roughness geometries: (a) Arc rib with multiple gaps [19]; (b) Symmetrical gap arc geometry and staggered element [21]; (c) Half symmetrical arc rib geometry; (d) Full symmetrical arc rib geometry.

Table 1. Range of roughness parameters of the proposed roughness geometries.

Roughness Parameters	Arc rib with multiple gaps [19]	Symmetrical gap arc geometry and staggered element [21]	Half symmetrical arc rib geometry	Full symmetrical arc rib geometry
e	2.3	2.3	2.3	2.3
g/e	4	4	3	3
g'/e	-	-	1	1
r/e	-	4	3	3
p/e	10	10	10	10
p'/p	-	0.4	0.4	0.4
Ng	6	6	8	6
n_g	-	-	8	5
d/w	-	0.65	0.65	0.65

experimental setup takes 2–2.5 hours to reach the steady state. Experimental data are collected only after the steady state is achieved. For each roughened plate the atmospheric air inlet temperature (T_i), absorber plate surface temperature (T_p) at various locations, hot air temperature (T_o) at the exit section and pressure drop (ΔP_d) in the test section at various m through the duct are measured and recorded in order to evaluate Nu , f and THPP.

3.1. Data compilation

The observed parameters (T_i , T_o , T_p and ΔP_d) are measured under steady-state conditions. For a certain Re these values are utilized to calculate Nu , f and THPP. The following relevant equations [21] are employed to compute air mass flow rate (m), useful heat gain through air (Q_{air}), convective heat transfer coefficient (h), Nusselt Number (Nu) and Friction factor (f):

$$m = C_d A_o \sqrt{\frac{2\rho_a(\Delta P)_o}{1 - \beta^4}}, \quad (1)$$

$$Q_{air} = mC_p(T_o - T_i), \quad (2)$$

$$h = \frac{mC_p(T_o - T_i)}{A(T_p - T_f)}, \quad (3)$$

$$Nu = \frac{hD_h}{k}, \quad (4)$$

$$f = \frac{2(\Delta P)_d D_h}{4\rho_a L V^2}. \quad (5)$$

The accuracy and precision of experimental result of different parameters are measured during the test run [28]. The maximum uncertainty in evaluated parameters is 1.77–1.84 %, 4.03–7.49 %, 3.49–5.13 % for Re , Nu and f respectively. The least count and uncertainty values in the measurement of duct and rib dimensions are 0.1 mm (Vernier Caliper) and ± 0.1 mm. A digital micro-manometer with the least count of 0.1 Pa and ± 0.1 Pa of uncertainty is used in the measurement of pressure drop along the test section. Uncertainty in the measurement of temperature (T-Type, Copper-constantan thermocouple) is $\pm 0.25^\circ\text{C}$ (Holman 1971). The least count and uncertainty in the measurement of voltage and current for the heating effect are 1% and ± 0.01 , respectively.

3.2. Validation of setup arrangement for smooth plate

Experimental results for smooth plates are compared with theoretical results obtained from correlations given in the literature. Dittus-Boelter [29] and Bhatti and Shah [30] correlations given by Eq. (6) and Eq. (7), respectively, represent the theoretical Nusselt number (Nu_{th_s}) and friction factor (f_{th_s}):

$$Nu_{th_s} = 0.023Re^{0.8}Pr^{0.4}, \quad (6)$$

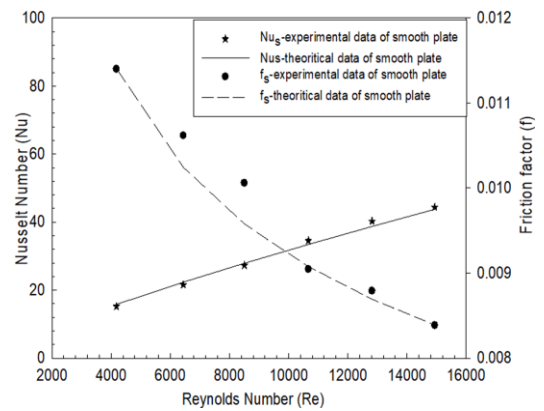
$$f_{th_s} = f_s + 0.0175\left(\frac{D_h}{L}\right), \quad (7)$$

$$f_s = \left(1.0875 - 0.1125\frac{H}{W}\right)f_o, \quad (8)$$

$$f_o = 0.0054 + 2.3 \times 10^{-8} Re^{1.5}, \quad (2100 \leq Re \leq 3550), \quad (9)$$

$$f_o = 1.28 \times 10^{-3} + 0.1143 Re^{-0.311}, \quad (3500 \leq Re \leq 10^7). \quad (10)$$

The experimental setup is validated using the Nu and f values for smooth plates obtained during the experimental run and the values of Nu and f obtained from correlations given in Eq. (6) and Eq. (7). Figure 4 indicates the variation of Nu and f with respect to Re for a smooth plate.


 Fig. 4. Experimental and theoretical values of Nu and f for a smooth plate for the validation of experimental set-up.

The absolute average variation between the Nu and f values obtained through correlations and the Nu and f values obtained during the experimental study is 3.98% and 4.87%, respectively. The accuracy of the fabricated experimental setup is ensured by a small difference between experimental findings and theoretical Nu and f values.

4. Physiognomic appearance of flowing fluids

An increase in the Nusselt number for artificial roughened geometry is due to variation in the air flow field near the roughened plate. Numerous investigators have reported the influence of arc rib roughness on h because of the development of flow vortices along arc rib and also the enlargement of secondary flow as shown in Fig. 5(a) for roughness geometry [19] in which only three types of flow are present main/primary flow flows over the arc shaped rib, flow through the main gap and the secondary flow developed along the arc rib. The main flow flows over the arc rib is responsible for the reattachment point between the two consecutive ribs, the main flow through the main gap is responsible for turbulence generation and the secondary flow along the rib acts to disrupt the formation of boundary layer along the rib element. For roughness geometry [21], the flow pattern underside of the absorber surface is shown in Fig. 5(b).

The staggered element in front of each main gap is used for scattering the main flow along the side of the staggered element

and to generate a turbulence zone between the free space of two consecutive main arc ribs. Applying the present roughness geometry, namely the full symmetrical arc rib results in a complex flow pattern near the roughened plate as shown in Fig. 5(c). The picture exhibits reattachment of the main flow behind the arc piece and segment element, secondary flow generation along the arc piece, secondary flow refreshment while passing through the gap, accelerating the main flow through an additional gap, secondary flow vortices generation, turbulence increase due to scattering of the main flow along the staggered rib and rapid mixing in turbulence wake region of the staggered rib. An additional gap in the symmetrical arc rib element accelerates the main flow and is scattered between the two consecutive staggered rib elements after passing through the gap and generates a turbulent region behind the main symmetrical arc rib element. Due to this, the area of wake region depresses.

An additional gap in the symmetrical arc rib element also hinders the formation of the secondary boundary sublayer along the arc rib. Acceleration in the main flow, scattering between the two consecutive staggered ribs and hindrance to the formation of the boundary sublayer along the arc rib element and its mixing with the main flow gives rise to the enhanced local Nu in the vicinity of a segment element downstream of the gap, leading to an increase in the average Nusselt number.

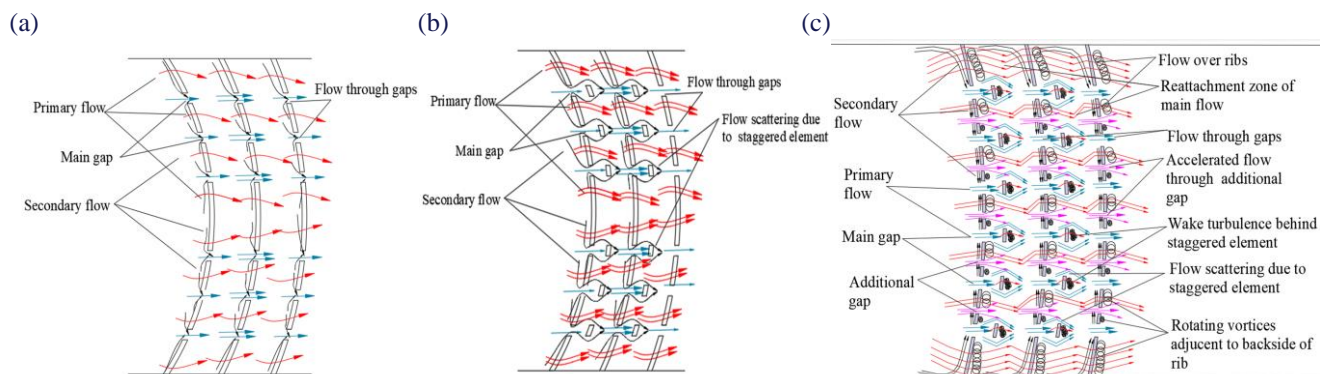


Fig. 5. Physiognomic appearance of flowing fluids over the test plate of different roughness geometries i.e.: (a) Arc rib with multiple gaps [19]; (b) Symmetrical gap arc geometry and staggered element [21]; (c) Full symmetrical arc rib geometry.

5. Experimental results and discussion

The current experimental analysis discloses the influence of the main gap, additional symmetrical gap and staggered element of half symmetrical arc rib geometry and full symmetrical arc rib geometry on h , f and THPP as shown in Figs. 6 to 8, respectively.

5.1. Variation of Nu and f with Re

Variation of Nu versus Re for the roughness geometries from [19, 21] and for two different proposed roughness geometries, namely half symmetrical arc rib geometry and full symmetrical arc rib geometry is shown in Fig. 6. A higher Re produces more turbulence that facilitates heat dissipation from the surface.

A high dissipation rate helps in achieving high Nu values. Nu increases with the increase in Re . The additional gap in the

symmetrical arc rib accelerates the main flow, thus increasing turbulence. According to Fig. 6, an increase in Nu values is a result of diminution in viscous sublayer thickness with the increase in Re . The ratio of Nu for a roughened absorber surface to Nu for a smooth surface (Nu/Nu_s) for [19, 21] and two different proposed roughness geometries mentioned above is between 1.54–2.01, 1.72–2.22, 1.66–2.06 and 1.90–2.36, respectively. The highest range for the Nu/Nu_s ratio is 1.90 to 2.36 for full symmetrical arc rib geometry for the entire range of investigated Re .

The additional enrichment in h observed for the staggered rib with an additional gap in the symmetrical arc rib element in the full symmetrical arc rib over the staggered rib with the symmetrical arc rib can be accredited to the accelerated flow of air through the small additional gap in the symmetrical arc rib as shown in Fig. 5(c). The accelerated flow gets scattered between

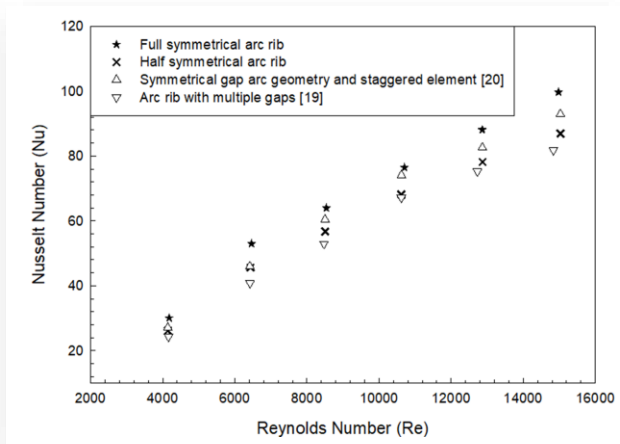


Fig. 6. Variation of Nu against Re at various roughness geometries.

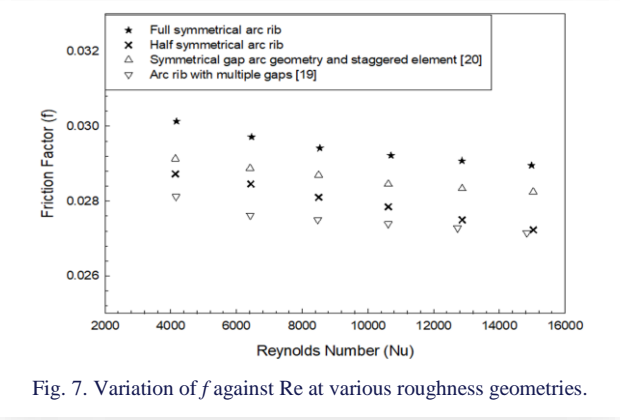


Fig. 7. Variation of f against Re at various roughness geometries.

the two consecutive staggered rib elements and generates a turbulent region behind the main symmetrical arc rib element. Due to this, the wake region depresses. The increment in the contact area between the flowing fluid and the heated plate between two consecutive ribs leads to a high h from the absorber surface.

The establishment of secondary flow along the arc rib element shows a considerable effect in disturbing the main flow. In the duct with arc rib roughness, the secondary flow is much stronger than compared to V-shaped rib roughness. The formation of boundary sub-layer along the arc rib shows an adverse effect on h . To suppress the effect of boundary sublayer, an additional gap is provided in the symmetrical arc rib, and due to this additional gap, a rise in the heat transfer rate is observed in comparison with the roughness geometry [19, 21].

The number of the main gaps N_g and the number of additional gaps n_g in half symmetrical arc rib roughness is 4, which means that the total number of main gaps N_g and additional gaps n_g of half symmetrical arc rib roughness is 8 over the span of the test plate as shown in Fig. 2(c) and Fig. 3(c), while the total number of main gaps N_g and additional gaps n_g in full symmetrical arc rib roughness is 6 and 5, respectively, over the span of the test plate as shown in Fig. 2(d) and Fig. 3(d). As the number of main gaps in the arc geometry increases, more free space between the consecutive rib elements are available for the main flow. The volume of flowing fluid passes through the free space without encountering the rib element increases. Turbulence in

the vicinity of the absorber surface decreases resulting low h is perceived. Vortices generation near the rough surface contributes to heat removal from the heated surface. The half symmetrical arc rib roughness provides more open spaces in total, increase area between the rib elements for the fluid flow. The flow passes through the wider area with a low velocity and without encountering the rib elements, leading to a lower intensity of turbulence generation near the absorber surface.

Variation of f versus Re is shown in Fig. 7. Re has an adverse influence on f . There is a pressure difference between the sides of the rib. Equation 5 clearly indicates the impact of pressure difference and air flow velocity on the friction factor (f). The pressure difference on both sides of the rib element and the air flow velocity inside the duct participate cumulatively to determine f . For the entire range of Re as 4 000–16 000, the ratio of f for the roughened absorber surface to f for the smooth surface (f/f_s) for [19, 21] and two different proposed roughness geometries, namely half symmetrical arc rib geometry and full symmetrical arc rib geometry is 2.46–3.23, 2.54–3.37, 2.51–3.25 and 2.64–3.45, respectively. The maximum f/f_s ratio is 2.64–3.45 for full symmetrical arc rib geometry for the entire range of investigated Re.

By investigating the roughness geometry of [19] and [21], from the experimental results it is evident that the friction factor increases by employing the staggered rib in front of the main gap as ΔP_d increases in the duct along the test length as shown in Fig. 7. An additional gap in the symmetrical arc rib for half symmetrical arc rib roughness shows a positive effect on the friction factor as the additional gap provides free space for the secondary flow and as well as for the main flow as the friction factor of half symmetrical arc rib roughness is lower than in [21]. The friction factor increases as an additional gap in the symmetrical arc rib for full symmetrical arc rib roughness is introduced. This is due to a lower number of N_g and n_g in full symmetrical arc rib roughness than in half symmetrical arc rib roughness and due to a high value of ΔP_d in the duct.

5.2. Effect of THPP

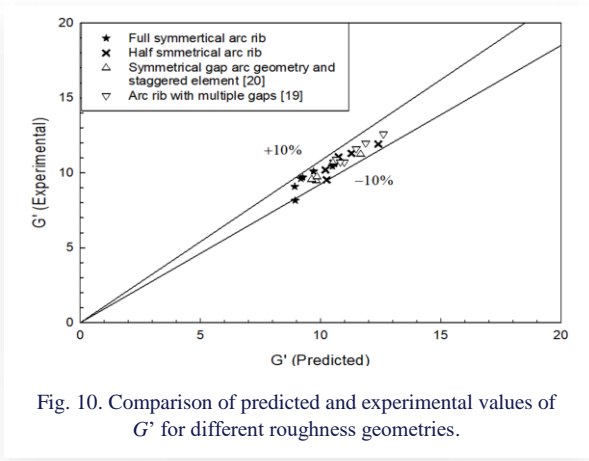
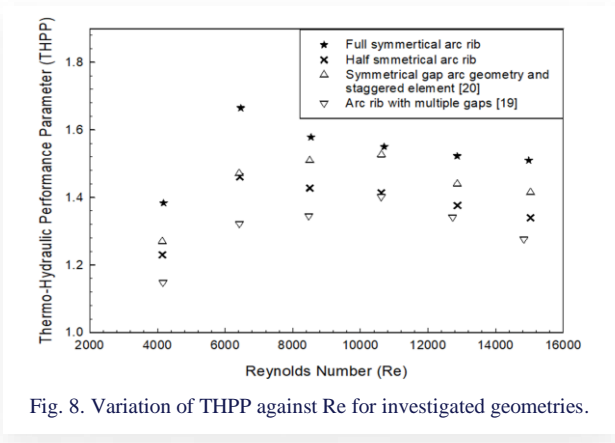
The thermal enhancement of a roughened SAH escalates the frictional losses. Hence, it is essential to conclude the thermal performance of a roughened SAH by considering both thermal and frictional characteristics at the same time. Webb and Eckert [31] suggested the thermal-hydraulic performance parameter (THPP) that considered both thermal characteristics in terms of Nusselt number and frictional characteristic in terms of friction factor of a rough surface with reference to the smooth surface.

$$THPP = \frac{Nu/Nu_s}{(f/f_s)^{1/3}} \tag{11}$$

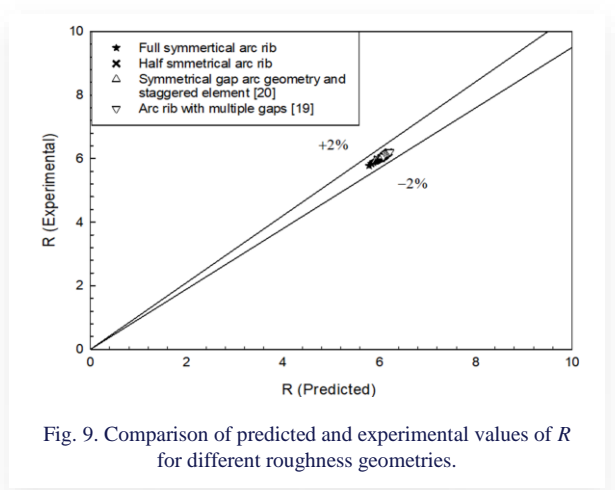
THPP higher than unity indicates the effectiveness of the SAH duct integrated with rib roughness. THPP is used to conclude the performance of various roughness geometry arrangements with respect to that of the smooth duct. Fig. 8 shows THPP versus Re.

The range of THPP variation is 1.14–1.40, 1.27–1.52, 1.23–1.46 and 1.38–1.66 for roughness geometries of [19, 21],

half symmetrical arc rib and full symmetrical arc rib. The maximum THPP is observed for the full symmetrical arc rib over the investigated range of Re. As Re increases, THPP increases and attains a maximum at Re equal to 6 000, then declines with the further increase in Re. The maximum variation of THPP is 1.38–1.66 for the full symmetrical arc rib.



SAH is shown in Fig. 11 followed by the step-by-step procedure (from Step 1 to Step 12) to calculate the thermal performance of a single pass roughened rectangular duct of SAH with the help of Eqs. (12) to (30).

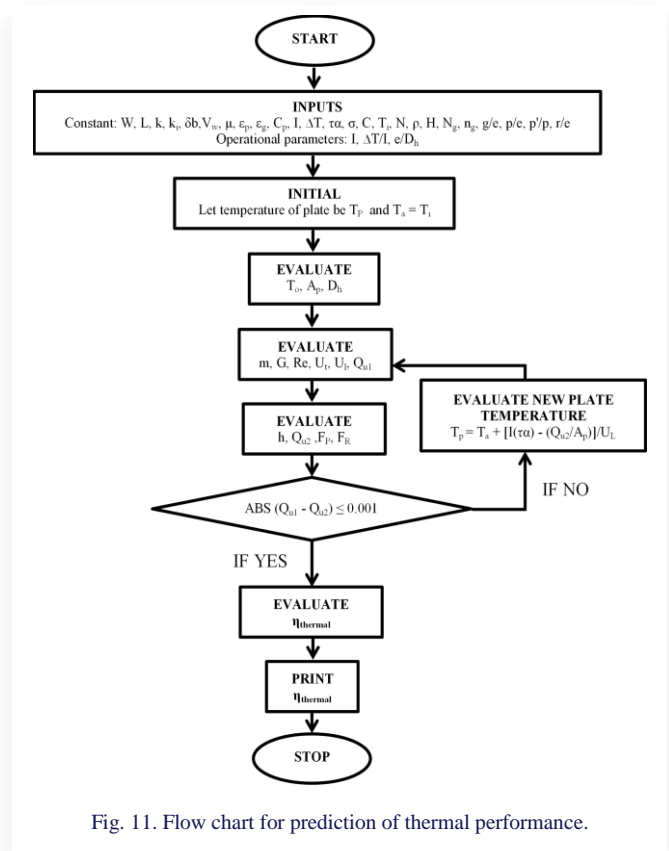


6. Correlation for R and G'

Empirical correlations have been developed by considering the combined effect of Re, e/D_h, e⁺, f on the roughness function (R) [32] and heat transfer function (G') [33] as represented in Appendix A. It is seen that the maximum deviation among the predicted values and experimental values of R and G' was ± 2 % and ± 10 %, respectively, as shown in Fig. 9 and Fig. 10.

7. Thermal performance prediction

Thermal performance prediction of a single pass roughened rectangular duct of SAH was done with the correlation developed for R and G' as shown in Table 3 given in Appendix A. The mathematical model is established to analyze the heat discharge in the system. Different surface heat losses such as Q_s, Q_b, and Q_r, roughness parameters, properties of fluid and other relevant parameters are the performance parameters used for numerical analysis to investigate the thermal behaviour of the system. A flow diagram for the prediction of thermal performance of



Step 1: The performance prediction is initiated with the selection of roughness and system parameters listed in Table 2.
 Step 2: The inlet air temperature (T_i) is considered the ambient air temperature (T_a) as ambient air at the inlet section is sucked by a solar air heater duct. The outlet temperature (T_o) at the exit section is determined by using the inlet temperature (T_i) and temperature increment along the duct (ΔT).

$$T_o = \Delta T + T_i \tag{12}$$

Table 2. Parameters used in the mathematical model for numerical analysis.

No.	System parameters	Values
1.	SAH duct channel parameters	$L = 1 \text{ m}$, $W = 0.3 \text{ m}$, $H = 0.025 \text{ m}$, $W/H = 12$
2.	Properties of insulating material of SAH duct	$k_i = 0.037 \text{ W/(mK)}$, $\delta_b = 0.05 \text{ m}$, $t_i = 0.05 \text{ m}$
3.	Parameters and properties of glass cover material of SAH duct	$N = 1$, $\varepsilon_g = 0.88$, $\tau\alpha = 0.80$
4.	Emissivity of test plate	$\varepsilon_p = 0.90$
5.	Solar intensity	$I = 1000 \text{ W/m}^2$
6.	Wind velocity	$V_w = 1 \text{ m/s}$
7.	Ambient temperature	$T_a = 300 \text{ K}$
8.	Relative artificial roughness height	$e/D_h = 0.0433$
9.	Investigated range of Reynolds number	$Re = 4\ 000\text{--}15\ 000$

Step 3: To estimate the heat transfer rate from the test plate to the air, i.e. useful heat gain, the plate temperature (T_p) is initialized by giving it some value.

Step 4: The heat loss coefficient (U_L) is found by summation of different side heat loss coefficients such as U_t , U_b and U_s of the rectangular SAH duct:

$$U_L = U_t + U_b + U_s, \quad (13)$$

$$U_b = \frac{k_i}{\delta_b}, \quad (14)$$

$$U_s = \frac{(L+W)t_e k_i}{LWt_i}. \quad (15)$$

The top heat loss coefficient U_t is a function of T_p , T_a and many other parameters and is computed using Eq. (16) as suggested by Klein [34]:

$$U_t = \left[\frac{N}{\left(\frac{C}{T_p}\right)^{N+f}} + \frac{1}{h_w} \right]^{-1} + \frac{\sigma(T_p^2 + T_a^2)(T_p + T_a)}{(\varepsilon_p + 0.00591Nh_w)^{-1} + \left[\frac{(2N+f-1) + 0.133\varepsilon_p}{\varepsilon_g} \right]^{-N}} \quad (16)$$

where:

$$f = (1 + 0.089h_w - 0.1166h_w\varepsilon_p)(1 + 0.07866N), \quad (17)$$

$$et = 0.43 \left(1 - \frac{100}{T_p} \right), \quad (18)$$

$$C = 520(1 - 0.000051s^2). \quad (19)$$

where s is the tilt of the collector (for a horizontal collector, $s = 0$). h_w is a function of wind velocity given by McAdams [35]:

$$h_w = 5.7 + 3.8V_w. \quad (20)$$

Step 5: The estimation of Qu_1 is done by Eq. (21):

$$Qu_1 = A_p [I(\tau\alpha) - U_L(T_p - T_a)]. \quad (21)$$

Step 6: The mass flow rate (m) as in Eq. (22), mass velocity (G) as in Eq. (23) and Re as in Eq. (24) are calculated as follows:

$$m = \frac{Qu_1}{C_p \Delta T}, \quad (22)$$

$$G = \frac{m}{WH}, \quad (23)$$

$$Re = \frac{GD_h}{\mu}. \quad (24)$$

Step 7: Eq. (31), Eq. (32) and Eq. (33) and values from Table 3 given in Appendix A govern G' and R . G' and R further used to quantify the Stanton number and subsequent Nu number.

Step 8: Calculation of h and F_p from Eq. (25) and Eq. (26):

$$h = \frac{kNu}{D_h}, \quad (25)$$

$$F_p = \frac{h}{h + U_L}. \quad (26)$$

Step 9: Calculation of F_o as below:

$$F_o = \frac{mC_p}{U_L A_p} \left[\exp\left(\frac{F_p U_L A_p}{mC_p}\right) - 1 \right]. \quad (27)$$

Step 10: Calculation of Qu_2 as below:

$$Qu_2 = F_o A_c [I(\tau\alpha) - U_L(T_o - T_a)]. \quad (28)$$

Step 11: Values of Qu_1 from Eq. (21) and Qu_2 are found from Eq. (28). If the deviation in values of Qu_1 and Qu_2 is higher than 0.1%, a new plate temperature (T_p)_n is determined by an iteration method using the equation as follows:

$$T_p = T_a + \frac{[I(\tau\alpha) - \frac{Qu_2}{A_p}]}{U_L}. \quad (29)$$

Step 12: η_{th} of SAH is evaluated using Eq. (30) after the plate temperature is found:

$$\eta_{th} = F_o \left[(\tau\alpha) - \frac{U_L(T_o - T_i)}{I} \right]. \quad (30)$$

The theoretical efficiency found from Eq. (30) is equated with the experimental thermal efficiency of SAH to validate the mathematical model.

Figure 12 illustrates the thermal efficiency found from the mathematical model versus the experimental thermal efficiency for the arc rib with multiple gaps [19], symmetrical gap arc geometry and staggered element [20] and arc rib with multiple gaps [19], half symmetrical arc rib and

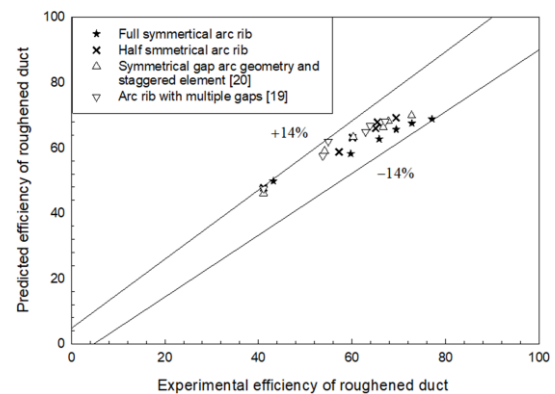


Fig. 12. Experimental and predicted thermal efficiencies for different roughness geometries.

full symmetrical arc rib. Figure 12 shows that for roughened surfaces, the deviations in thermal efficiencies found from the mathematical model and the experimental run lie within $\pm 14\%$, indicating that the suggested mathematical model may be utilized to estimate SAH thermal performance.

8. Conclusions

The aim of the present investigation is to identify a way to enhance the heat transfer of the best arc rib geometry as per the literature, which is restricted by boundary layer rebuilding along its considerable long continuous arc segment. By adding another gap in the continuous arc segment, this unrestricted boundary layer redevelopment can be terminated. Investigating experimental results, novel arc rib roughness geometry outperforms in comparison to best arc rib geometry as per the literature. Novel arc rib geometry is the scientific contribution of the current study. To determine the impact of the proposed roughness geometry, namely, half symmetrical arc rib and full symmetrical arc rib geometry on h , f , and THPP, an experimental examination using a rectangular SAH duct with W/H of 12 has been carried out. The conclusions are as follows.

1). Half symmetrical arc rib and full symmetrical arc rib geometry show significant enhancement in heat transfer rate (h) with respect to the smooth duct.

2). The additional gap in the symmetrical arc rib elements influences the Nu and f values. The ranges of highest increment with respect to the smooth plate in Nu and f are 1.90–2.36 and 2.64–3.45 times, respectively, for full symmetrical arc rib geometry, while the increment in Nu and f values for half symmetrical arc rib geometry is 1.66–2.06 and 2.51–3.25, respectively.

3). The range of THPP for the full symmetrical arc rib and half symmetrical arc rib is 1.38–1.66 and 1.23–1.46, respectively.

4). THPP of existing roughness geometries of [19] and [21] has also been studied experimentally. It was found that the range of THPP for these geometries is 1.14–1.40 and 1.27–1.52, respectively, while the range of THPP for full symmetrical arc rib geometry (present study) is 1.38–1.66. Thus, the present study has the highest THPP for full symmetrical arc rib geometry, which is 1.66.

5). A correlation has been developed between G' and e^+ as well as between R and e^+ . The maximum deviation in the experimental and theoretical values of R and G' is $\pm 2\%$ and $\pm 10\%$, respectively.

6). The present mathematical model has been validated by comparing the thermal efficiency obtained from the mathematical model and from results obtained by experimental run.

Future research may be accompanied by investigating the effect of various geometrical constraints like p/e , p'/p , Ng , ng , d/w , r/e , e/D_h to better understand the overall behaviour of half symmetrical arc rib and full symmetrical arc rib geometries on the performance of SAH. Practically, it is tedious work to explore all parameters experimentally, so flow simulations can also be

considered to investigate the flow patterns resulting from using half symmetrical arc rib and full symmetrical arc rib geometries.

Appendix A. Correlation development

Several investigators have established empirical correlations for the heat transfer coefficient and friction factor for a roughened SAH. The roughness function (R) given as in Eq. (31) and the roughness Reynolds number (e^+) given as in Eq. (32) is suggested by Nikurade [32]. The dimensionless flow velocity represented by R , in a control volume with enclosed edge roughness elements, shows the momentum loss caused by roughness. The single dimensionless indicator e^+ is used to represent optimum conditions for characterizing the performance of rough surface and flow parameters:

$$R = \sqrt{\frac{2}{f}} + 2.5 \ln \left(\frac{2e}{D_h} \right) + 3.75, \quad (31)$$

$$e^+ = \text{Re} \left(\frac{e}{D_h} \right) \sqrt{\frac{f}{2}}. \quad (32)$$

The dimensionless heat transfer function (G') given by Eq. (33) indicates the competence of the rough surface in terms of heat transfer and temperature difference for the same controlled volume:

$$G' = \left[\left(\frac{f}{2St} \right) - 1 \right] \sqrt{\frac{2}{f}} + R. \quad (33)$$

Table 3. Constant coefficients for R and G' for investigated geometries.

Roughness Geometry	$R = C(e^+)^{C_0}$		$G' = C_1 + C_2(e^+) + C_3(e^+)^2$		
	C	C_0	C_1	C_2	C_3
Full symmetrical arc rib	5.3963	0.0224	10.6712	-0.0883	0.0011
Half symmetrical arc rib	5.4398	0.0297	12.8759	-0.1355	0.0017
Symmetrical gap arc geometry and staggered element [21]	5.6085	0.0174	13.0714	-0.1575	0.0018
Arc rib with multiple gaps [19]	5.7535	0.0181	15.1026	-0.1980	0.0022

Figure 13 represents R versus e^+ for an arc rib with multiple gaps [19], symmetrical gap arc geometry and staggered element [21], half symmetrical arc rib and full symmetrical arc rib. Eq. (31) and Fig. 13 indicate that R takes lower values for higher values of f . Figure 7 shows the highest f for the full symmetrical arc rib and Fig 13 shows a lower R for the full symmetrical arc rib.

Figure 14 represents G' versus e^+ for an arc rib with multiple gaps [19], symmetrical gap arc geometry and staggered element [21], half symmetrical arc rib and full symmetrical arc rib. Eq. (33) and Fig. 14 indicate lower G' at higher Nu, and Fig. 6 confirms that the highest Nu occurs for the full symmetrical arc rib and the lowest G' for the same full symmetrical arc rib.

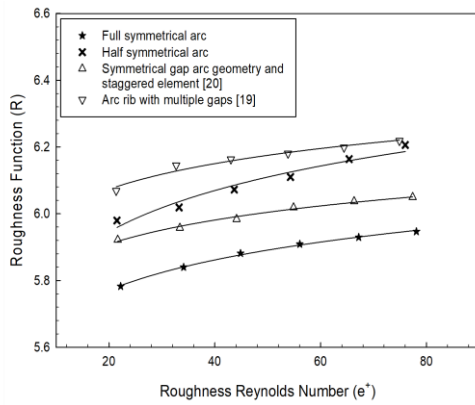


Fig. 13. Variation of R versus e^+ for investigated geometries.

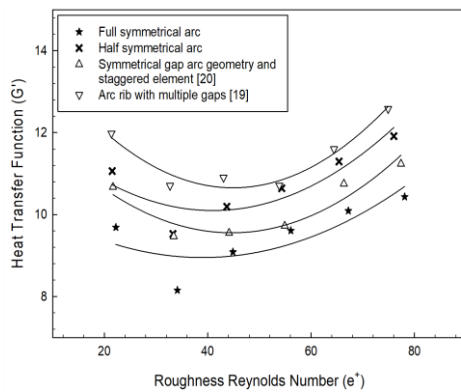


Fig. 14. Variation of G' versus e^+ for investigated geometries.

Correlations between R and e^+ and G' and e^+ are developed for an arc rib with multiple gaps [19], symmetrical gap arc geometry and staggered element [21], half symmetrical arc rib and full symmetrical arc rib. All roughness geometries have distinct coefficients and power indexes in the developed correlations between R and e^+ and between G' and e^+ , as listed in Table 3.

Acknowledgements

The authors are extremely grateful to Maulana Azad National Institute of Technology Bhopal for providing experimentation amenities to accomplish this research work.

References

[1] Haldar, A., Varshney, L., & Verma, P. (2022). Effect of roughness parameters on performance of solar air heater having artificial wavy roughness using CFD. *Renewable Energy*, 184, 266–279. doi: 10.1016/j.renene.2021.11.088

[2] Bhuvad, S.S., Azad, R., & Lanjewar, A. (2022). Thermal performance analysis of apex-up discrete arc ribs solar air heater-an experimental study. *Renewable Energy*, 185, 403–415. doi: 10.1016/j.renene.2021.12.037

[3] Arunkumar, H.S., Kumar, S., & Vasudeva Karanth, K. (2022). Performance enhancement of a solar air heater using rectangular perforated duct inserts. *Thermal Science and Engineering Progress*, 34, 101404. doi: 10.1016/j.tsep.2022.101404

[4] Sureandhar, G., Srinivasan, G., Muthukumar, P., & Senthilmurugan, S. (2022). Investigation of thermal performance in a solar air heater having variable arc ribbed fin configuration. *Sustainable Energy Technologies and Assessments*, 52(PA), 102069. doi: 10.1016/j.seta.2022.102069

[5] Dheeraj Kumar, A.L. (2022). Nusselt number and friction characteristics of solar air heater roughened with novel twisted V-shaped staggered ribs using liquid crystal thermography. *Renewable Energy*, 110, 131932. doi: 10.1016/j.renene.2022.11.007

[6] Ravi, R.K., & Saini, R.P. (2016). Experimental investigation on performance of a double pass artificial roughened solar air heater duct having roughness elements of the combination of discrete multi V shaped and staggered ribs. *Energy*, 116, 507–516. doi: 10.1016/j.energy.2016.09.138

[7] Ravi, R.K., & Saini, R.P. (2018). Nusselt number and friction factor correlations for forced convective type counter flow solar air heater having discrete multi V shaped and staggered rib roughness on both sides of the absorber plate. *Applied Thermal Engineering*, 129, 735–746. doi: 10.1016/j.applthermaleng.2017.10.080

[8] Abbas, S., Yuan, Y., Hassan, A., Zhou, J., Ji, W., Yu, T., Rehman, U.U., & Yousuf, S. (2022). Design a low-cost, medium-scale, flat plate solar air heater: An experimental and simulation study. *Journal of Energy Storage*, 56, 105858. doi: 10.1016/j.est.2022.105858

[9] Zhang, Q., Wang, T., Hou, Q., Song, K., & Hu, W. (2022). Case Studies in Thermal Engineering Thermal hydraulic performance augmentation by petal-shaped ribs in a two-pass cooling channel. *Case Studies in Thermal Engineering*, 40, 102542. doi: 10.1016/j.csite.2022.102542

[10] Ayalew, Y.G. (2022). Experimental Investigation of Heat and Fluid Flow Characteristics on Expanded Metal Mesh Roughened Solar Collector. *Trends in Sciences*, 19(22).

[11] Salih, H.M. (2022). A comparative study for double pass solar air collector utilizing medial glass panel. *Archive of Mechanical Engineering*, 69(4), 729–747. doi: 10.24425/ame.2022.141524

[12] Jain, P.K., & Lanjewar, A. (2022). Experimental study of thermal augmentation in solar air heater roughened with aligned gaps in V-rib roughness with staggered element geometry. *Heat and Mass Transfer*, 58(4), 531–559. doi: 10.1007/s00231-021-03118-6

[13] Patel, L.A., & Singh, S. (2019). Experimental and numerical investigation of solar air heater with novel V rib. *Journal of Energy Storage*, 21.

[14] Karwa, R. (2003). Experimental studies of augmented heat transfer and friction in asymmetrically heated rectangular ducts with ribs on the heated wall in transverse, inclined, v-continuous and v-discrete pattern. *International Communications in Heat and Mass Transfer*, 30(2), 241–250. doi: 10.1016/S0735-1933(03)00035-6

[15] Saini, S.K., & Saini, R.P. (2008). Development of correlations for Nusselt number and friction factor for solar air heater with roughened duct having arc-shaped wire as artificial roughness. *Solar Energy*, 82(12), 1118–1130. doi: 10.1016/j.solener.2008.05.010

[16] Singh, A.P., Goel, V., Vashishtha, S., & Kumar, A. (2016). Heat Transfer Enhancement in a Solar Air Heater with Roughened Duct Having Arc-Shaped Elements as Roughness Element on the Absorber Plate. *Journal of the Institution of Engineers: Series C*, 97(3), 381–388. doi: 10.1007/s40032-016-0240-2

[17] Hans, V.S., Gill, R.S., & Singh, S. (2017). Heat transfer and friction factor correlations for a solar air heater duct roughened artificially with broken arc ribs. *Experimental Thermal and Fluid Science*, 80, 77–89. doi: 10.1016/j.expthermflusci.2016.07.022

- [18] Gill, R.S., Hans, V.S., Saini, J.S., & Singh, S. (2017). Investigation on performance enhancement due to staggered piece in a broken arc rib roughened solar air heater duct. *Renewable Energy*, 104, 148–162. doi: 10.1016/j.renene.2016.12.002
- [19] Jain, S.K., Agrawal, G.D., & Misra, R. (2020). Experimental investigation of thermohydraulic performance of the solar air heater having arc-shaped ribs with multiple gaps. *Journal of Thermal Science and Engineering Applications*, 12(1), 1–10. doi: 10.1115/1.4044427
- [20] Azad, R., Bhuvad, S., & Lanjewar, A. (2021). Study of solar air heater with discrete arc ribs geometry: Experimental and numerical approach. *International Journal of Thermal Sciences*, 167, 107013. doi: 10.1016/j.ijthermalsci.2021.10701
- [21] Ambade, J., & Lanjewar, A. (2019). Experimental investigation of solar air heater with new symmetrical GAP ARC GEOMETRY and staggered element. *International Journal of Thermal Sciences*, 146, 106093. doi: 10.1016/j.ijthermalsci.2019.106093
- [22] Jain, P.K., Lanjewar, A., & Bhagoria, J.L. (2022). Heat transfer analysis of double discrete arc roughness with different relative rib altitudes and relate to a single discrete arc in the solar air heater. *International Journal of Ambient Energy*, 43(1), 6806–6828. doi: 10.1080/01430750.2022.2052959
- [23] Singh, A.P., Varun, & Siddhartha. (2014). Effect of artificial roughness on heat transfer and friction characteristics having multiple arc shaped roughness element on the absorber plate. *Solar Energy*, 105, 479–493. doi: 10.1016/j.solener.2014.04.007
- [24] Agrawal, Y., Bhagoria, J.L., Gautam, A., Kumar Chaurasiya, P., Arockia Dhanraj, J., Muthiya Solomon, J., & Salyan, S. (2022). Experimental evaluation of hydrothermal performance of solar air heater with discrete roughened plate. *Applied Thermal Engineering*, 211, 118379. doi: 10.1016/j.applthermaleng.2022.118379
- [25] Pandey, N.K., Bajpai, V.K., & Varun. (2016). Experimental investigation of heat transfer augmentation using multiple arcs with gap on absorber plate of solar air heater. *Solar Energy*, 134, 314–326. doi: 10.1016/j.solener.2016.05.007
- [26] Kumar, R., Goel, V., Singh, P., Saxena, A., Kashyap, A.S., & Rai, A. (2019). Performance evaluation and optimization of solar assisted air heater with discrete multiple arc shaped ribs. *Journal of Energy Storage*, 26, 100978. doi: 10.1016/j.est.2019.100978
- [27] ASHRAE. (1977). Standard, Method of Testing to Determine the Thermal Performance of Solar Collector (93–97). ASHRAE.
- [28] Kline, S.J., & McClintock, F. (1953). Describing uncertainties in single sample. *Mechanical Engineering*, 75, 3–8.
- [29] Rosenhow, W.M., & Hartnett, J.P. (1973). *Handbook of Heat Transfer*. Mc Graw Hill. New York.
- [30] Bhatti, M.S., & Shah, R.K. (1987). Turbulent and transition flow convective heat transfer. In *Handbook of Single-Phase Convective Heat Transfer* (pp. 4.1–4.166). Wiley. doi: 10.1016/0255-2701(88)87007-7
- [31] Webb, R.L., & Eckert, E.R.G. (1972). Application of rough surfaces to heat exchanger design. *International Journal of Heat and Mass Transfer*, 15(9), 1647–1658. doi: 10.1016/0017-9310(72)90095-6
- [32] Nikuradse, J. (1950). Laws of Flow in Rough Pipes. *NACA, Technical Memorandum 1292*. doi: 10.1016/s0882-6110(18)30184-6
- [33] Dipprey, D.F., & Sabersky, R.H. (1963). Heat and momentum transfer in smooth and rough tubes at various Prandtl numbers. *International Journal of Heat and Mass Transfer*, 6(5), 329–353. doi: 10.1016/0017-9310(63)90097-8
- [34] Klein, S.A. (2018). Calculation of flat-plate collector loss coefficients. In *Renewable Energy*, Chapter 29 (1st ed.). Routledge. London. doi: 10.4324/9781315793245
- [35] McAdams, W.H. (1954). *Heat Transmission*. McGraw Hill. New York.